Supporting Information

Amine-Silane-Induced Ag-Cu Dendrites on Al/ZnO: An Integrated SERS Monitoring and Photodegradation Platform for Triphenylmethane Dyes

Lixia Qin*, Hui Shen, Taiyang Zhang, Shi-Zhao Kang, Xiangqing Li*

Faculty of Chemical Engineering and Energy Technology, Shanghai Institute of Technology, 100 Haiquan Road, Shanghai 201418, China

E-mail: lxqin@sit.edu.cn (Lixia Qin); xqli@sit.edu.cn (Xiangqing Li)

Contents:

Chemicals and Materials

Aluminium metal sheet (99.5%, 0.2 mm thickness) and copper metal sheet (99.5%, 0.2 mm thickness) were purchased from Tianjin Fuchen Metal Materials Co. Ltd. Sodium hydroxide (NaOH, 96%), hexamethylene tetramine ($C_6H_{12}N_4$, 99.99%), zinc nitrate hexahydrate ($Zn(NO_3)_2 \cdot 6H_2O$, 98%), APTES (98%), silver nitrate ($AgNO_3$, 99.99%) and copper(II) nitrate trihydrate ($Cu(NO_3)_2 \cdot 3H_2O$, 99%) were purchased from Adamas, Titan Scientific Co. Ltd. Brilliant Green (BG, $C_{27}H_{34}N_2O_4S$, 95%), crystal violet (CV, $C_{25}H_{30}ClN_3$, 90%), bright blue (BB, $C_{37}H_{34}N_2NaO_9S_3$, 85%), thiram (TM, $C_6H_{12}N_2S_4$, 98%), tetracycline hydrochloride (T-H, $C_{22}H_{24}N_2O_8 \cdot HCl$, 99%), bromocresol purple (BCP, $C_{21}H_{16}Br_2O_5S$, 98%), bromocresol green (BCG, $C_{21}H_{14}Br_4O_5S$, 95%), malachite green (MG, $C_{23}H_{25}ClN_2$, 98%), methyl orange (MO, $C_{14}H_{14}N_3NaO_3S$, 98%), methyl red (MR, $C_{15}H_{15}N_3O_2$, 92%), phenol red (PR, $C_{19}H_{14}O_5S$, 99%), rhodamine 6G (R6G, $C_{28}H_{31}ClN_2O_3$, 99%), rhodamine B (RhB, $C_{28}H_{31}ClN_2O_3$, 95%), 4-aminothiophenol (4-ATP, C_6H_7NS, 97%), isopropyl alcohol (IPA, 99%), benzoquinone (BQ, 99%) and ammonium oxalate (AO, 99%) were purchased from Adamas, Titan Scientific Co. Ltd.

Characterizations

Scanning electron microscope (SEM) images, element distribution image and Energy-dispersive X-ray spectroscopy (EDX) were obtained by ZEISS Gemini 300. transmission electron microscope (TEM) images and high-resolution TEM (HRTEM) images were taken by JEM-2100F. X-ray photoelectron spectroscopy (XPS) were measured by Shimadzu/Krayos AXIS Ultra DLD. X-ray diffraction (XRD) patterns were measured by Rigaku Ultima IV. Fourier transform infrared spectroscopy (FTIR) were measured by Thermo Scientific Nicolet iS20. Raman and SERS spectra were measured by a i-Raman spectrophotometer (Thermo Scientific DXR, BWS465-532S). Photocurrent spectra and electrochemical impedance spectra (EIS) were taken by electrochemistry workstation (CHI660E). The measurement of solid diffusion reflection UV-Vis absorption spectra were made by UV-3900 spectrophotometer.

Photocatalytic degradation experiment was carried out with mercury lamp as light source (CEL-M500). Mott-Schottky curve was taken by electrochemistry workstation (CHI760E). Total organic carbon (TOC) was conducted by Shimadu TOC-L. Electron paramagnetic resonance (EPR) spectra were measured by Bruker EMXplus-6/1.

The stability, repeatability and uniformity of the Al/ZnOA/Ag-Cu substrate

To assess the stability, the Al/ZnOA/Ag-Cu substrates with the same batch were cut into several pieces and stored for different days (1, 3, 5, 7, 14, 21, 28 and 90), respectively. Then, 20 μL of 1×10^{-6} mol·L^{-1} BG solution was dripped onto the Al/ZnOA/Ag-Cu substrate at the corresponding time, and all the SERS signals were detected randomly at different spots. Also, six batches of the Al/ZnOA/Ag-Cu substrates were obtained, and SERS signals of 10 points in each batch were randomly collected to study the repeatability of the substrates. Furthermore, 20 μL of 1×10^{-6} mol·L^{-1} BG solution was dripped onto the substrate (2 cm × 2 cm) and SERS signals of 36 points were randomly collected for evaluating the uniformity of the Al/ZnOA/Ag-Cu substrate.

Preparation of real fish tissue samples

Fresh muscle tissue from grass carp was obtained from a local market. Specifically, 1.0 g of the minced tissue was accurately weighed and transferred into a 15 mL centrifuge tube. Then, 5.0 mL of an extraction solvent (e.g., 80% acetonitrile in water, v/v) was added. The mixture was vigorously vortexed for 2 mins and subsequently ultrasonicated in a water bath for 15 mins at room temperature. After centrifugation at 10,000 rpm for 10 mins, the supernatant was collected and passed through a 0.22 μm nylon syringe filter. The filtrate was appropriately diluted with phosphate buffer (10 mM, pH 7.4) prior to SERS analysis. For the fish pond water samples, they were simply filtered through a 0.22 μm membrane filter and used directly without further pretreatment.

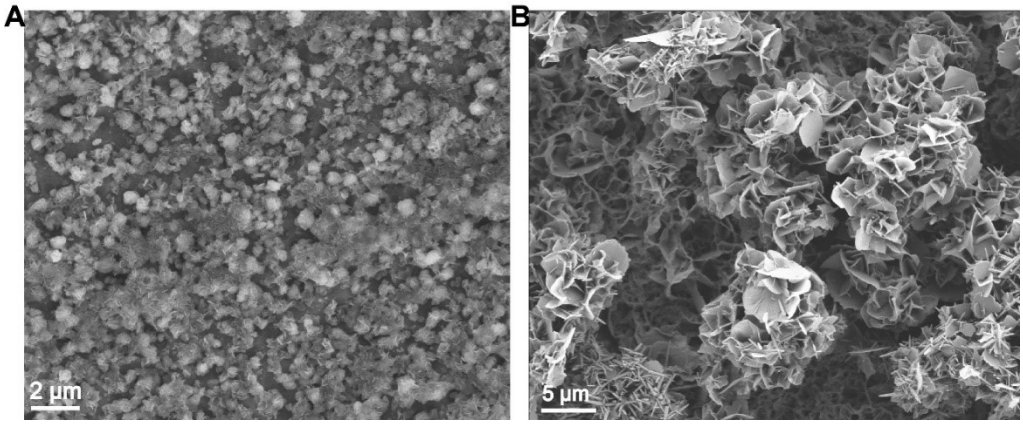

Fig. S1 SEM images of the etched Al (A) and (B) ZnO on unetched Al sheet.

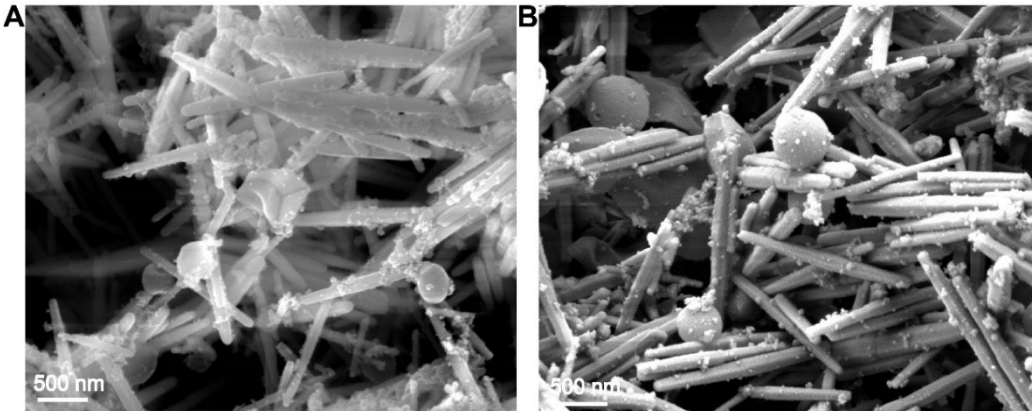

Fig. S2 SEM images of Al/ZnOA/Ag (A) and Al/ZnOA/Cu (B).

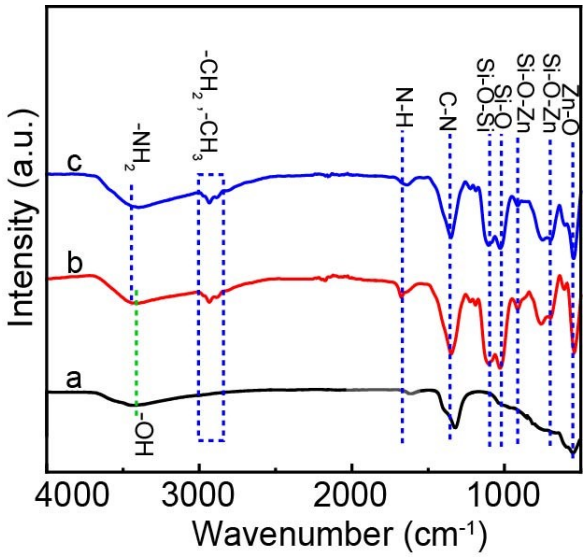

Fig. S3 FTIR spectra of Al/ZnO (a), Al/ZnOA (b) and Al/ZnOA/Ag-Cu (c) substrates.

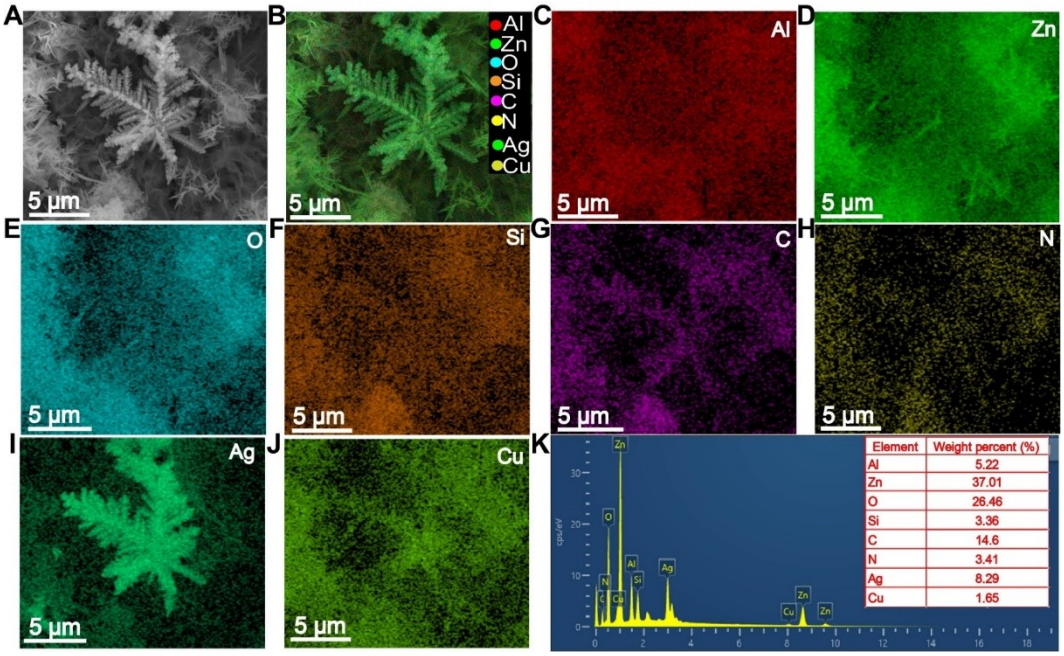

Fig. S4 The SEM image of the Al/ZnOA/Ag-Cu (A) and the superimposed map of all elements (B); The corresponding elemental distribution images: Al (C), Zn (D), O (E), Si (F), C (G), N (H), Ag (I) and Cu (J); EDX of the Al/ZnOA/Ag-Cu (K).

As shown in Figs. S5A and B (inset), after adsorption of 1×10^{-5} mol·L^{-1} BG for 1 h, the mass percentages of N and C increase from 3.4 % and 24.2 % to 28.6 % and 32.62 %, respectively, indicating that BG molecules are adsorbed on the Al/ZnOA/Ag-Cu. Also, after the adsorption of BG on the Al/ZnOA/Ag-Cu, the peaks of Ag 3d at 373.48 eV, 373.02 eV, 367.65 eV and 366.98 eV shift to 374.08 eV, 373.58 eV 368.08 eV and 367.58 (Fig. S5C), respectively. In addition, as illustrated in Fig. S5D, the peaks at 960.74 eV and 940.74 eV corresponding to the peaks of Cu^{2+} disappear completely, proving that the oxidation of Cu can be efficiently prevented by the adsorption of BG. Meanwhile, the peaks at 952.87 eV and 932.91 eV shift to 953.06 eV and 933.19 eV, respectively. Furthermore, it can be seen from the high resolution XPS spectrum of N 1s that the peak at 399.19 eV shifts to 399.79 eV, and also a new peak at 401.90 eV is observed which assigns to N-$(C)_3$ of BG molecules (Fig. S5A). These above results demonstrate that BG molecules are adsorbed on the Al/ZnOA/Ag-Cu and also there exists the strong binding ability between the Al/ZnOA/Ag-Cu and BG.[1] Meanwhile,

driven by the above strong interaction, the chemical environment changes of the substrate and the obvious displacement of C, Zn and Si elements are also observed before and after adsorption of 1 × 10^{-5} mol·L^{-1} BG (Figs. S5B, 5E and 5F). Therefore, more BG molecules will easily approach the Al/ZnOA/Ag-Cu substrate by the strong chemical binding, and thus SERS response is greatly enhanced.

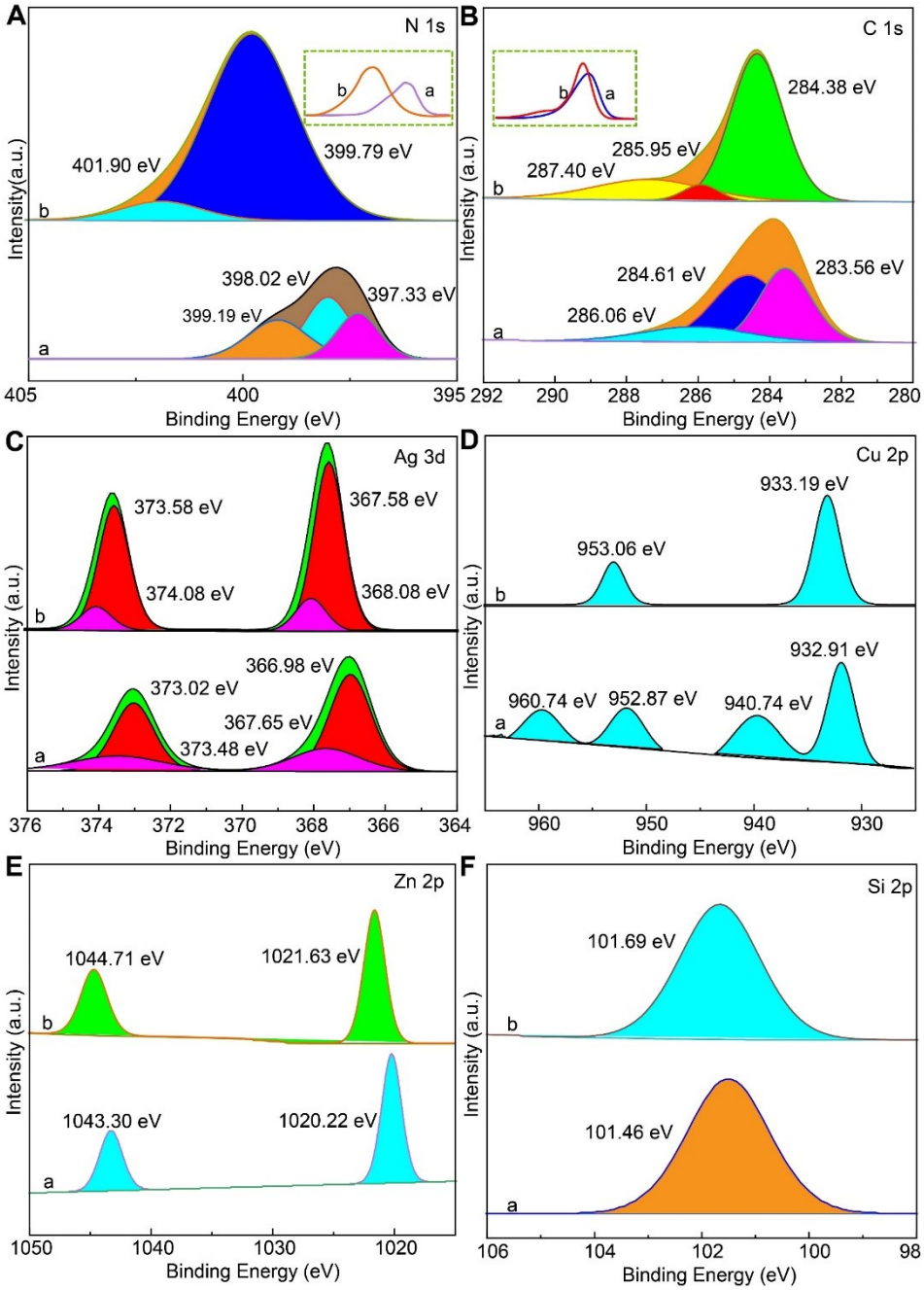

Fig. S5 HRXPS spectra of N 1s (A), C 1s (B), Ag 3d (C), Cu 2p (D), Zn 2p (E) and Si 2p (F) in the Al/ZnOA/Ag-Cu before (a) and after (b) adsorption of 1 × 10^{-5} mol·L^{-1} BG for 1 h.

Table S1 Comparative SERS EFs for different substrates using BG as the probe.

Substrate	EF	EF Ratio (vs. Al/ZnOA/Ag-Cu)	Key design feature
Al/ZnOA/Ag-Cu	4.08×10^7	1: 1	APTES-induced dendritic Ag-Cu alloy
Al/ZnO/Ag-Cu	2.72×10^7	1.5: 1	Ag-Cu without APTES (non-branched)
Al/ZnOA/Ag	1.41×10^7	2.9: 1	Single metal (Ag) only
Al/ZnOA/Cu	N/D	N/D	Single metal (Cu) only (signal below detection)
Al/Ag-Cu	2.47×10^6	16.5: 1	Non-branched Ag-Cu on Al sheet

Note: EF Ratio = EF(Al/ZnOA/Ag-Cu) / EF(Substrate). "N/D" (Not Determinable) indicates the SERS signal was indistinguishable from background noise, underscoring the lack of effective enhancement for the Cu-only substrate.

SERS substrates	Target analytes	LOD (mol·L^{-1})	References
Ag/ZnO	CV	1×10^{-13}	[2]

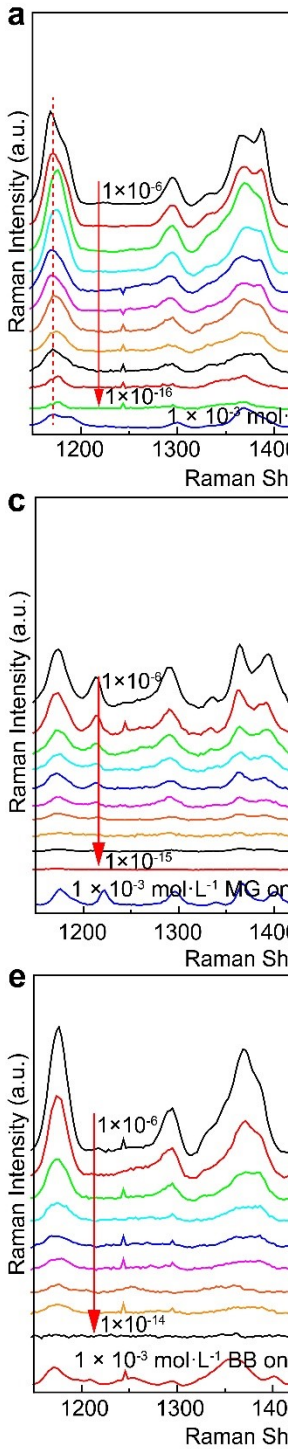

Fig. S6 (A, C and E) Raman spectra of dyes (1×10^{-3} mol·L^{-1}) on Al sheet and their SERS spectra with different concentrations on the Al/ZnOA/Ag-Cu substrate and (B, D and F) the corresponding SERS intensities at typical bands as a function of the negative logarithm of the concentration.

Ag-ZnO	R6G	1×10^{-9}	[3]
ZnO@Ag	TCS	1×10^{-9}	[4]
Ag@Ga-doped ZnO	R6G	1×10^{-12}	[5]
3D-porous ZnO/Ag	CV	1×10^{-9}	[6]
3D Ag/ZnO	PR	1×10^{-10}	[7]
Ag@ZnO-CuO	R6G	1×10^{-9}	[8]
Ag NFs@ZnO	CV	1×10^{-13}	[9]
3D ZnO/Ag	CV	1×10^{-11}	[10]
Al/ZnOA/Ag-Cu	BG	9.83×10^{-18}	Our work
Al/ZnOA/Ag-Cu	CV	1.04×10^{-17}	Our work
Al/ZnOA/Ag-Cu	MG	2.01×10^{-16}	Our work
Al/ZnOA/Ag-Cu	BB	1.26×10^{-15}	Our work

Table S2 The comparisons of various substrates toward pollutants detection.

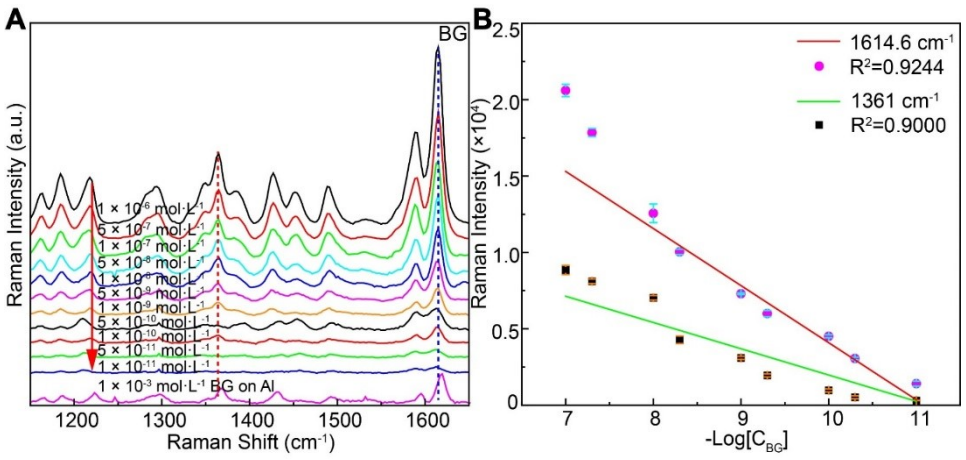

Fig. S7 (A) Raman spectrum of BG (1×10^{-3} mol·L^{-1}) on Al sheet and SERS spectra of BG

with different concentrations on Al/ZnO/Ag-Cu substrate; (B) The corresponding SERS intensities at typical bands as a function of the negative logarithm of BG concentration.

Table S3 Detailed assignment of characteristic SERS peaks for TPM dyes.

Compound	Observed SERS shift (cm^{-1})	Vibrational mode assignment	Ref.
BG	1614.6	ring C-C stretching vibration	[11]
	1361.3	phenyl-N-stretching	[11]
	1181.5	in-plane ring C-H bend	[11]
CV	1619.4	ring C-C stretching vibration	[12,13]
	1368.9	phenyl-N-stretching	[12,13]
	1176.3	in-plane ring C-H bend	[12,13]
MG	1614.6	ring C-C stretching vibration	[14]
	1361.3	N-phenyl stretching	[14]
	1173.7	ring C-H bending	[14]
BB	1619.5	ring C-C stretching vibration	[12,13]
	1368.8	phenyl-N-stretching	[12,13]
	1176.3	in-plane ring C-H bend	[12,13]

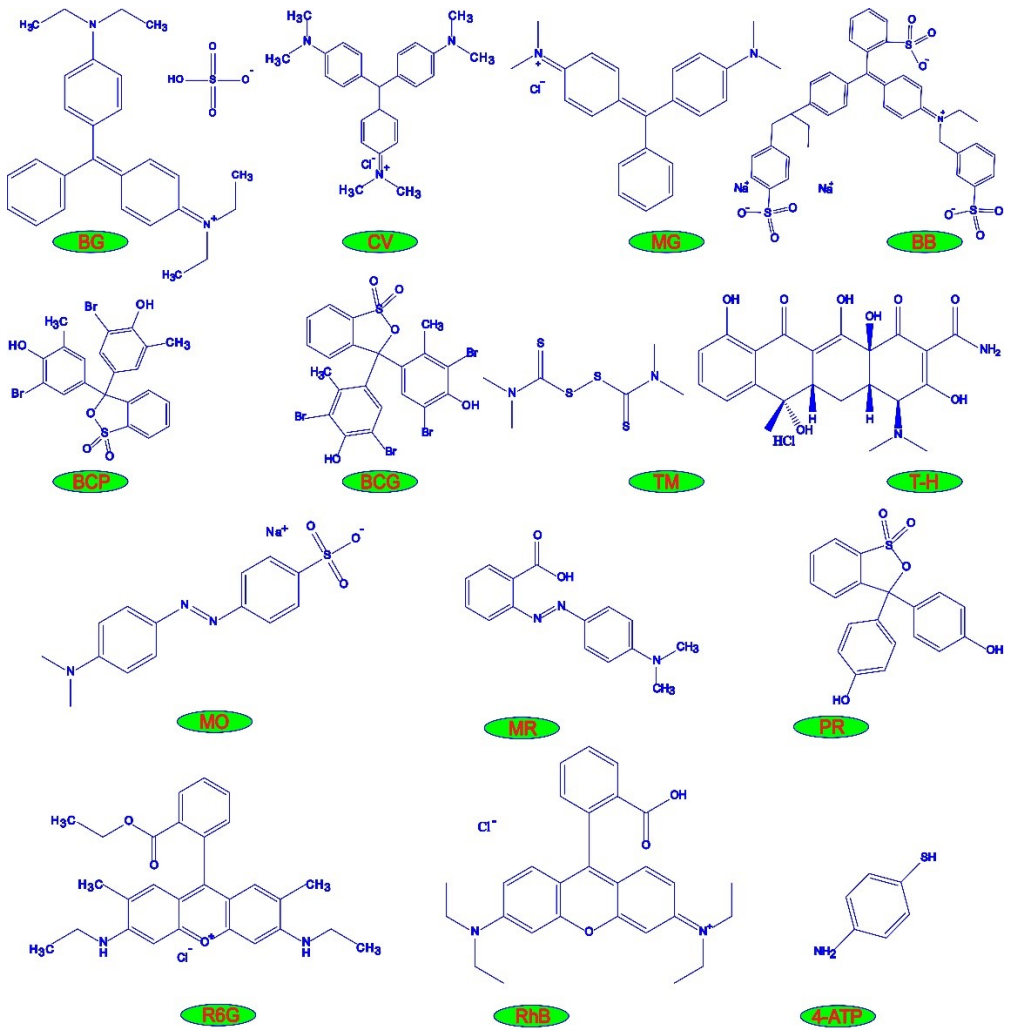

Fig. S8 The structures of BG, CV, TM, T-H, BCP, BCG, LCV, LMG, MO, MR, PR, R6G, RhB and 4-ATP.

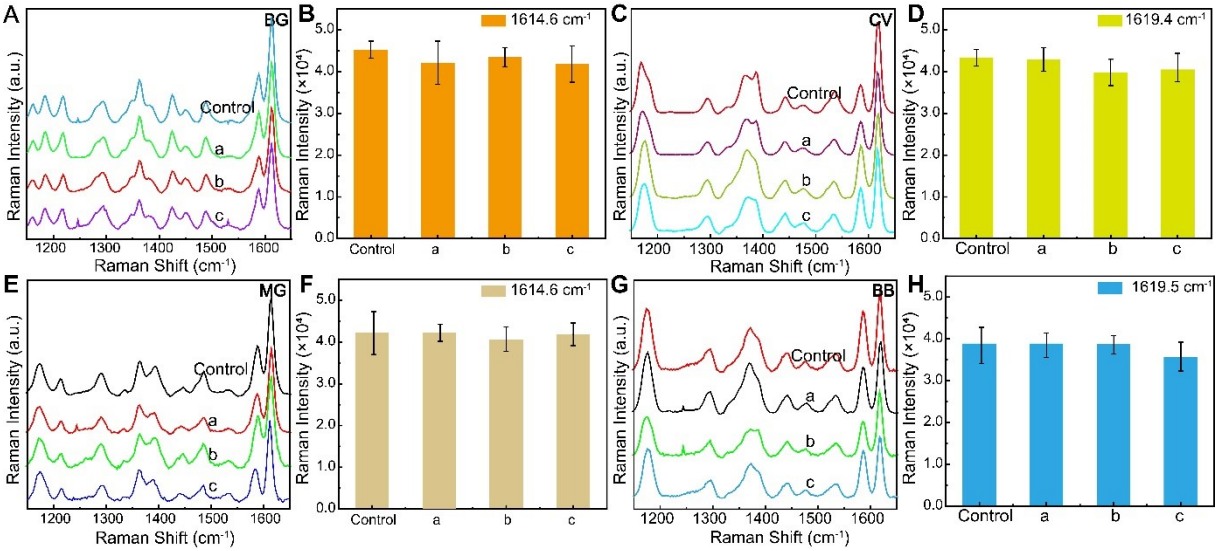

Fig. S9 Interference study with mixed interferents. SERS spectra (left panels) and peak intensity histograms (right panels) for (A, B) BG, (C, D) CV, (E, F) MG, and (G, H) BB. For each target (1×10^{-6} mol·L^{-1}): control (pure target) and three mixtures: (a) with BCP, BCG, TM, T-H; (b) with MO, MR, PR; (c) with R6G, RhB, 4-ATP. Each interferent in the mixtures was at 1×10^{-6} mol·L^{-1}.

Table S4 Recovery results for BG, CV, MG and BB spiked in fish extracts solution (n = 3).

Compound	Spiked concentration (mol·L^{-1})	Found concentration (mol·L^{-1})	Recovery (%)	RSD (%)
BG	3.16×10^{-7}	$3.29 \pm 0.22 \times 10^{-7}$	104.11	6.69
	3.16×10^{-8}	$3.05 \pm 0.17 \times 10^{-8}$	96.52	5.57
	3.16×10^{-9}	$2.76 \pm 0.12 \times 10^{-9}$	87.34	4.35
	3.16×10^{-10}	$2.58 \pm 0.09 \times 10^{-10}$	81.65	3.49
CV	3.16×10^{-7}	$3.25 \pm 0.21 \times 10^{-7}$	102.85	6.46
	3.16×10^{-8}	$3.07 \pm 0.10 \times 10^{-8}$	97.15	3.26
	3.16×10^{-9}	$2.89 \pm 0.16 \times 10^{-9}$	91.46	5.54
	3.16×10^{-10}	$2.57 \pm 0.06 \times 10^{-10}$	81.33	2.33
MG	3.16×10^{-7}	$3.31 \pm 0.25 \times 10^{-7}$	104.75	7.55
	3.16×10^{-8}	$3.06 \pm 0.15 \times 10^{-8}$	96.84	4.90
	3.16×10^{-9}	$2.83 \pm 0.20 \times 10^{-9}$	89.56	7.07
	3.16×10^{-10}	$2.62 \pm 0.14 \times 10^{-10}$	82.91	5.34
BB	3.16×10^{-7}	$3.45 \pm 0.26 \times 10^{-7}$	109.18	7.54
	3.16×10^{-8}	$3.01 \pm 0.18 \times 10^{-8}$	95.25	4.90
	3.16×10^{-9}	$2.75 \pm 0.22 \times 10^{-9}$	87.03	7.07
	3.16×10^{-10}	$2.59 \pm 0.11 \times 10^{-10}$	81.96	4.25

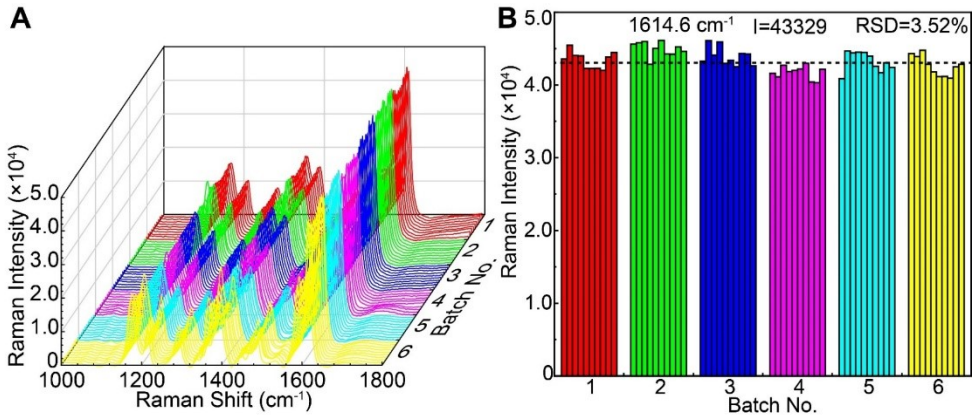

Fig. S10 (A) SERS signals of 1 × 10^{-6} mol·L^{-1} BG on different batches of the Al/ZnOA/Ag-Cu substrates and (B) the corresponding histograms of SERS intensity at 1614.6 cm^{-1}.

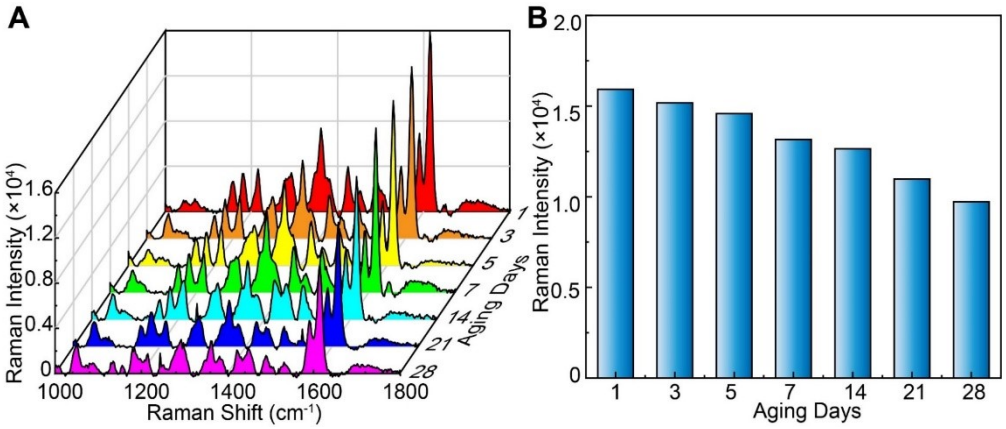

Fig. S11 (A) SERS signals of BG (1 × 10^{-6} mol·L^{-1}) on Al/ZnOA/Ag substrate within 28 days and (B) the corresponding histograms of SERS intensities at 1614.6 cm^{-1}.

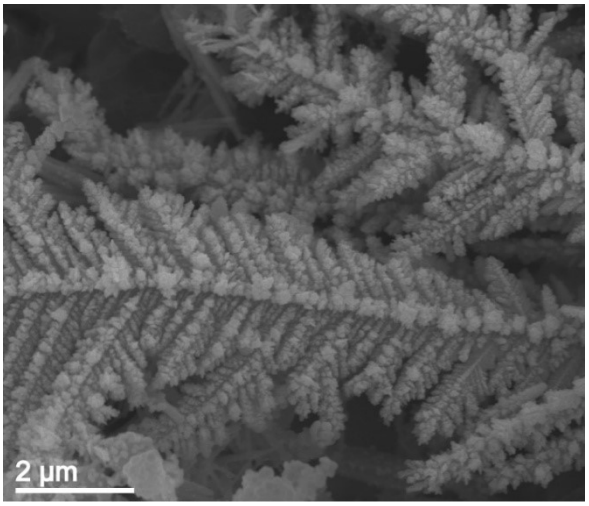

Fig. S12 SEM image of Al/ZnOA/Ag-Cu after five cycles of photocatalytic degradation.

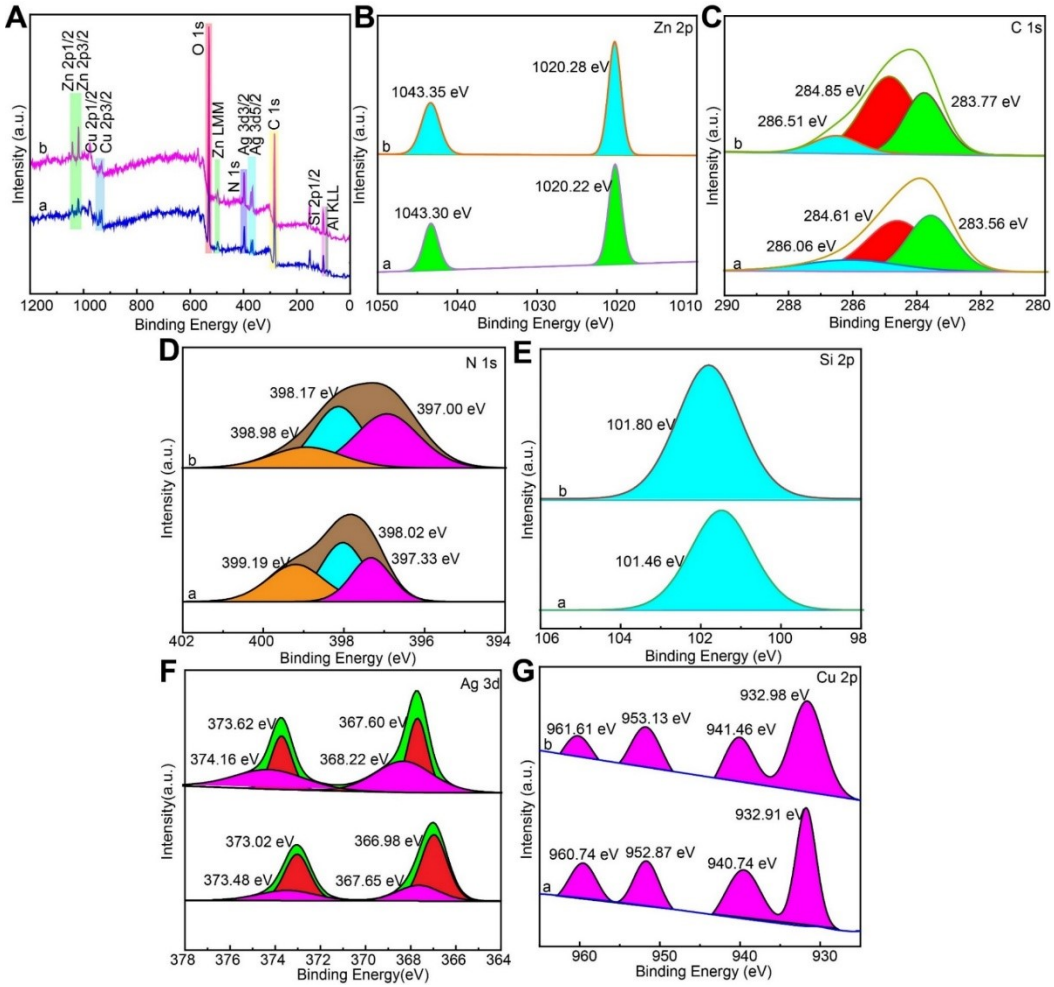

Fig. S13 (A) The survey XPS spectra and HRXPS spectra of Zn 2p (B), C 1s (C), N 1s (D), Si 2p (E), Ag 3d (F) and Cu 2p (G) in the Al/ZnOA/Ag-Cu before (a) and after (b) five cycles of photocatalytic degradation.

The morphology and valence states of the Al/ZnOA/Ag-Cu after five cycles of photocatalytic degradation were characterized by SEM and XPS, respectively. As shown in Fig. S12, after five cycles of photocatalytic degradation, it is evident that the dendritic bimetallic Ag-Cu distributed on the surface of the Al/ZnOA substrate is still observed. As depicted in Fig. S13 (A-G), the survey XPS of all elements and HRXPS spectra of Zn 2p, C 1s, N 1s, Si 2p, Ag 3d and Cu 2p in the Al/ZnOA/Ag-Cu demonstrate that the valence states have no significant changes after five cycles of photocatalytic degradation. It verifies that the Al/ZnOA/Ag-Cu substrate is with excellent stability for photocatalytic degradation of BG.

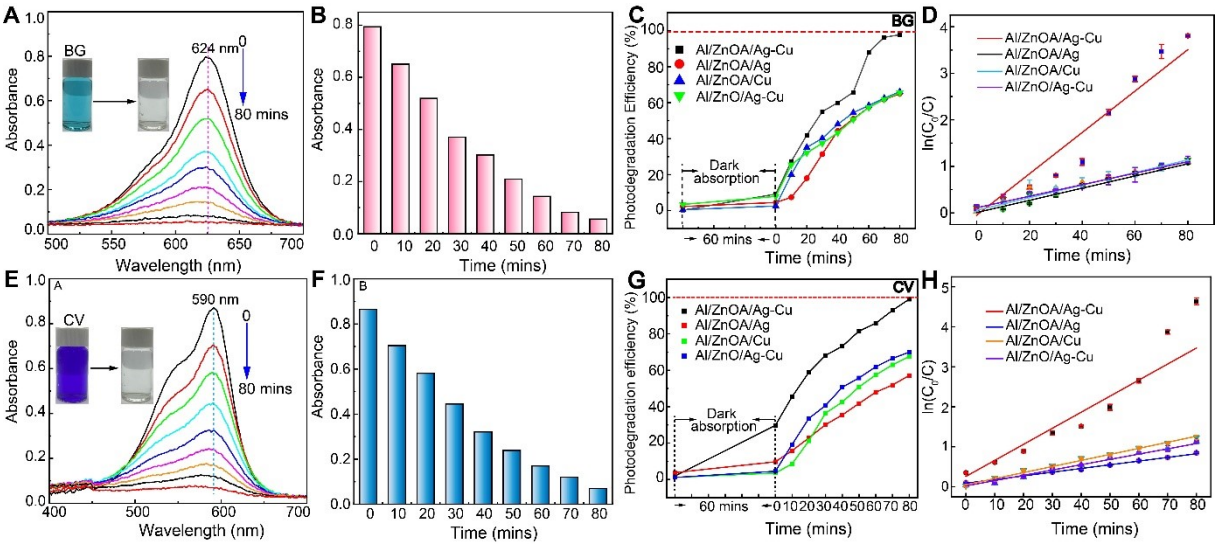

Fig. S14 Photocatalytic degradation and mechanistic control experiments. Top row (A-D): Degradation of BG. (A) Time-dependent UV-Vis absorption spectra of BG solution (1×10^{-5} mol·L^{-1}). (B) Corresponding absorbance decay at 624 nm. (C) Photocatalytic degradation efficiency of BG over time on different substrates. (D) Pseudo-first-order kinetic plots derived from (C). Bottom row (E-H): Degradation of CV. (E) Time-dependent UV-Vis absorption spectra of CV solution (1×10^{-5} mol·L^{-1}). (F) Corresponding absorbance decay at 590 nm. (G) Photocatalytic degradation efficiency of CV over time on different substrates. (H) Pseudo-first-order kinetic plots derived from (G).

The photocatalytic efficiency of the Al/ZnOA/Ag-Cu substrate was first evaluated using BG. As shown in Fig. S14A and S14B, the characteristic absorption peak of BG at 624 nm diminishes rapidly under simulated sunlight, with a degradation efficiency of 97.76% achieved within 80 min. This high activity is further confirmed with CV, the degradation of which is nearly complete (99.02%) under identical conditions, as monitored by the decay of its absorption at 590 nm (Fig. S14E, F).

To systematically elucidate the roles of the APTES layer and the Ag-Cu synergy, control experiments with substrates lacking key components were performed. For BG degradation (Fig. S14C, D), the Al/ZnOA/Ag-Cu substrate significantly outperformed the controls: Al/ZnOA/Ag (67.75 %), Al/ZnOA/Cu (66.05 %), and Al/ZnO/Ag-Cu (65.47 %). Its pseudo-first-order rate

constant ($k = 0.050\ min^{-1}$) was 3.57, 3.85, and 4.17 times higher than those of the respective controls. An identical trend is observed for CV degradation (Fig. S14G, H). The Al/ZnOA/Ag-Cu composite exhibits a rate constant of $0.040\ min^{-1}$, which is 4.44 times that of Al/ZnOA/Ag, 2.67 times that of Al/ZnOA/Cu, and 3.07 times that of Al/ZnO/Ag-Cu.

These comparative results provide clear evidence for the proposed mechanism: (1) The APTES layer is crucial, as its absence (in Al/ZnO/Ag-Cu) leads to markedly inferior performance, confirming its role in forming the active dendritic alloy structure. (2) A synergistic effect between Ag and Cu exists, since the bimetallic alloy consistently and substantially outperforms either single-metal counterpart (Al/ZnOA/Ag or Al/ZnOA/Cu). The superior activity of the Al/ZnOA/Ag-Cu architecture is therefore attributed to the strong interfacial coupling facilitated by APTES and the efficient charge separation enabled by the Ag-Cu synergy.

Table S5 Comparison of photocatalytic performance for the degradation of TPM dyes.

Various substrates	Pollutants	Rate constant	Degradation time and efficiency	Ref.
NiO-ZnO	CV	$0.0033\ min^{-1}$	105 mins, 60%	[15]
MoO_3-ZnO	CV	$0.0191\ min^{-1}$	140 mins, 93.92%	[16]
Sn-ZnO (5%)	CV	$0.046\ min^{-1}$	120 mins, 93.1%	[17]
ZnO/Ag_2S	CV	-	120 mins, 94.1%	[18]
LP-ZnO	CV	-	150 mins, 100%	[19]
ZnO@CP2	CV	-	110 mins, 74.7%	[20]
CZ3/CSAC	BG	$0.022\ min^{-1}$	120 mins, 93.09%	[21]
Ag@CdO	BG	$0.030\ min^{-1}$	125 mins, 95.5%	[22]
PANI/Ni^0 NCs	BG	$0.039\ min^{-1}$	120 mins, 91.9%	[23]
Sn-ZnO/CSAC	BG	$0.027\ min^{-1}$	120 mins, 96.52%	[24]
Al/ZnOA/Ag-Cu	BG	$0.050\ min^{-1}$	80 mins, 97.76%	Our work
Al/ZnOA/Ag-Cu	CV	$0.040\ min^{-1}$	80 mins, 99.02%	Our work

Table S6 Comparison of recent representative SERS-photocatalytic platforms for pollutants treatment.

Platform (Material)	Design Strategy/Key Feature	SERS Performance (LOD)	Photocatalytic Performance	Application Demonstrated	Refs.
Al/ZnOA/Ag-Cu	APTES-induced in-situ growth of dendritic Ag-Cu alloy; Dual Ag-N/Cu-N channels for selective detection & catalysis.	~ 10^{-14} mol·L^{-1} (BG, in fish extract)	> 97 % (80 min, k = 0.050 min^{-1}, simulated sun light)	Unified detection & degradation; Specificity & accuracy in complex matrix.	This work
Ag/GO/ TiO_2 film	A synergistic effect of three components; with good self-cleaning and reusable properties.	~ 10^{-12} mol·L^{-1} (R6G)	~ 66 % (90 min, Xenon lamp)	Detection or degradation of R6G in aqueous solution	[25]
$Ni(OH)_2$/Ag powder	A simple and rapid in-situ deposition method to coat AgNPs onto flower-like $Ni(OH)_2$ spheres.	~ 10^{-8} mol·L^{-1} (MB, in east lake water)	> 90 % (120 min, k = 0.037 min^{-1}, simulated solar light)	Photocatalytic degradation with SERS tracking	[26]
Fe_3O_4@mTiO_2-Ag NS-Cs composite	Synergistic combination of "hot spot" effects and interfacial charge transfer	~ 10^{-11} mol·L^{-1} (antibiotics, in lake water, fish)	~ 92 % (90 min, Xenon lamp)	Photocatalytic process with SERS tracking	[27]

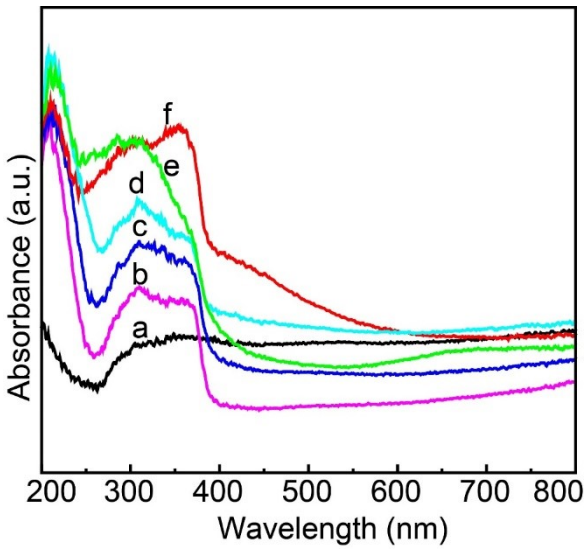

Fig. S15. Solid diffuse reflectance UV-Vis absorption spectra of (a) Al, (b) Al/ZnO, (c) Al/ZnOA, (d) Al/ZnOA/Ag, (e) Al/ZnOA/Cu and (f) Al/ZnOA/Ag-Cu.

In order to analyze the photocatalytic degradation mechanism of Al/ZnOA/Ag-Cu substrate for TPM dyes, the optical and photoelectrochemical properties were evaluated. As shown in Fig. S15, the solid diffuse reflectance UV-Vis absorption spectra of the Al, Al/ZnO, Al/ZnOA, Al/ZnOA/Ag, Al/ZnOA/Cu and Al/ZnOA/Ag-Cu were characterized. As shown in Fig.S15-b, the light absorption edge of Al/ZnO located at ~ 400 nm is found, and a slight shift to longer wavelength is observed in the Al/ZnOA after APTES is introduced (Fig. S15-c). Particularly, in comparison with a single metal decorated Al/ZnOA/Ag (Fig. S15-d) or Al/ZnOA/Cu (Fig. S15-e), the photo-response of bimetallic dendritic Ag-Cu loaded Al/ZnOA is remarkably enhanced in the visible light region of 400 ~ 700 nm, hence capable of absorbing more photons for photocatalytic degradation of pollutants.[28] It is attributed to the enhanced interfacial adhesion between Al/ZnO and dendritic Ag-Cu by means of the APTES.

Besides, the electrochemical measurements including of photocurrent response and impedance spectroscopy were performed to confirm the advantages of the Al/ZnOA/Ag-Cu in facilitating charge separation. As shown in Fig. S16A, the Al/ZnOA/Ag-Cu shows strong transient photocurrent response under irradiation, which is much higher than those of Al/ZnOA/Ag, Al/ZnOA/Cu and Al/ZnO/Ag-Cu, suggesting a highly enhanced charge separation in the Al/ZnOA/Ag-Cu.[29] As shown in Fig. S16B, in comparison with those of Al/ZnOA/Ag, Al/ZnOA/Cu and Al/ZnO/Ag-Cu, the arc radius of Al/ZnOA/Ag-Cu is significantly reduced, demonstrating the smaller resistance of charge transfer. Results indicate that the APTES can be used as channels of electron transfer for promoting the electron transport by the strong interface adhesion between Al/ZnO and the dendritic Ag-Cu.

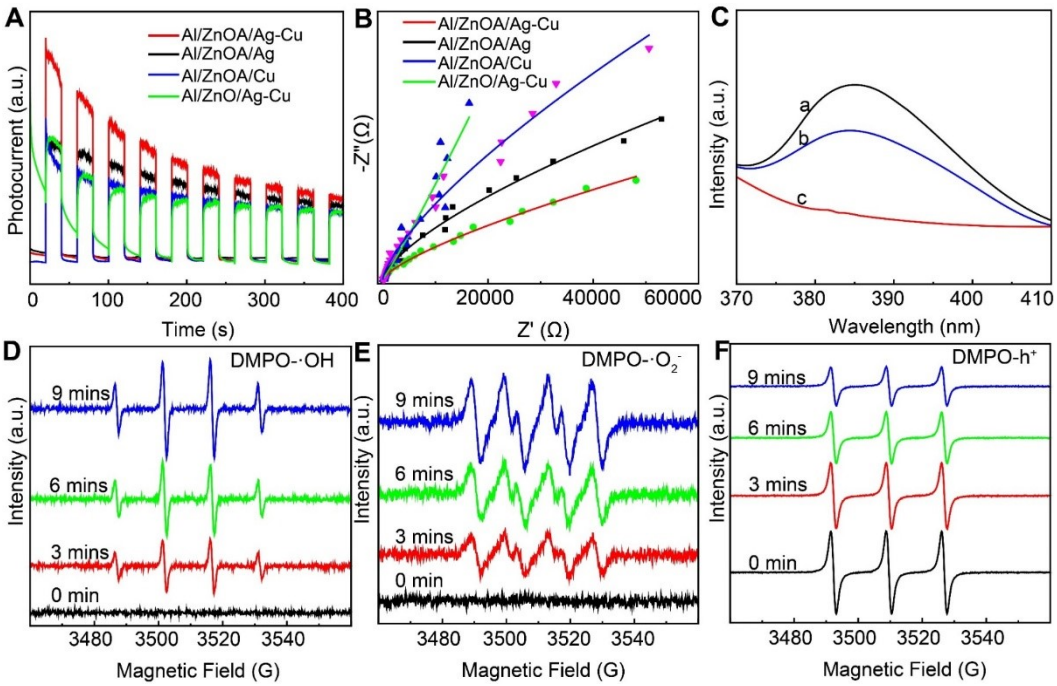

Fig. S16 (A) Photocurrent response; (B) Nyquist plots of electrochemical impedance spectra and (C) Fluorescence spectra of Al/ZnO (a), Al/ZnOA (b) and Al/ZnOA/Ag-Cu (c), λ_{ex} = 325 nm; (D-F) EPR spectra for ·OH, $\cdot O_2^-$ and h^+ at different times (0, 3, 6 and 9 mins).

For further exploring the separation efficiency of photoinduced electron-hole pairs in the substrates, fluorescence spectra of Al/ZnO, Al/ZnOA and Al/ZnOA/Ag-Cu were analyzed. As depicted in Fig. S16C-a, Al/ZnO has a strong emission peak at 385 nm (λ_{ex} = 325 nm). However, the fluorescence intensity of Al/ZnO at 385 nm obviously decreases after introducing APTES on the Al/ZnO (Fig. S16C-b). Furthermore, when the dendritic Ag-Cu is introduced on Al/ZnOA (Fig. S16C-c), the fluorescence of Al/ZnOA is almost completely quenched, demonstrating that the efficiency of charge transfer is significantly improved.[30] These results verify that the introduction of APTES and the formation of the dendritic Ag-Cu in the Al/ZnOA/Ag-Cu can offer more separation sites of charges, and inhibit the recombination of electrons and holes, which is conducive to the enhancement of photocatalytic activity.[31]

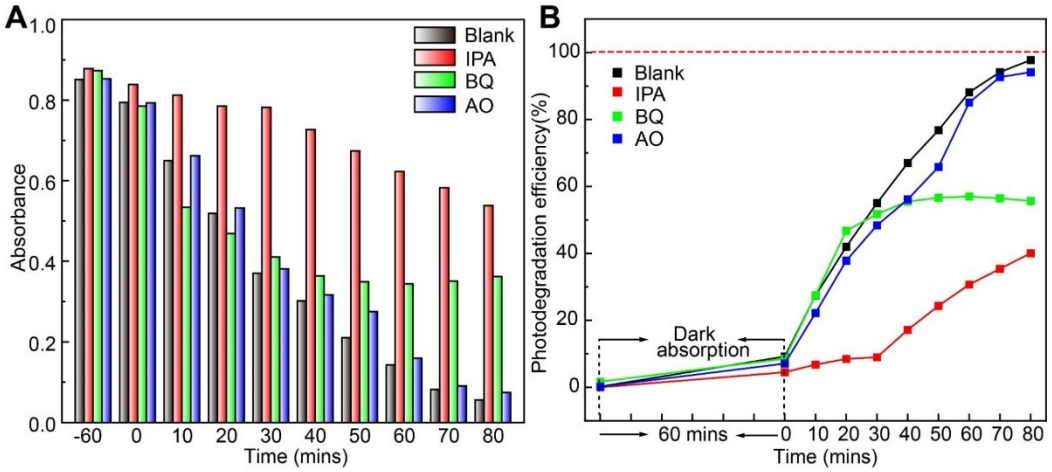

Fig. S17 (A) The absorbance of BG solution (1×10^{-5} mol·L^{-1}) at 624 nm on the Al/ZnOA/Ag-Cu substrate at different degradation times without scavenger and with free radical scavengers; (B) The photocatalytic degradation efficiency of BG (1×10^{-5} mol·L^{-1}) on Al/ZnOA/Ag-Cu substrate in 80 mins with and without scavengers.

As shown in Fig. S17A, in comparison with the blank (no scavengers added), the absorbance of the BG decreases slowly after the addition of IPA, BQ or AO scavengers. Especially, it is observed that the addition of IPA or BQ exhibits a significant inhibitory effect on the reduction of the absorbance. Besides, in the presence of IPA, BQ and AO, the photocatalytic degradation efficiencies of Al/ZnOA/Ag-Cu substrate for BG are 40.06 %, 55.66 % and 94.16 % within 80 mins, respectively (Fig. S17B). These above results demonstrate that ·OH and $\cdot O_2^-$ radicals are the dominate reactive species during the photocatalytic degradation of BG by the Al/ZnOA/Ag-Cu substrate.

The conduction behavior of Al/ZnOA and its flat-band potential (E_{FB}) are acquired according to the tangent of the Mott-Schottky curve. As shown in Fig. S18A, the E_{FB} of Al/ZnOA is the X-axis intercept of prolonging tangent that is evaluated to be -1.00 V vs. Ag/AgCl. For n-type semiconductor, the conduction band (CB) of Al/ZnOA is calculated to be -0.80 eV vs Ag/AgCl, which is equivalent to -1.00 eV vs NHE.[32] Furthermore, according to the band gap ($E_g = 3.10$ eV, obtained by the plot of $(\alpha h\nu)^2$ *vs* $h\nu$) (Fig. S18B) and the formula $E_g = E_{VB} - E_{CB}$, the potential value of the valence band (E_{VB}) can be calculated as 2.10 eV.

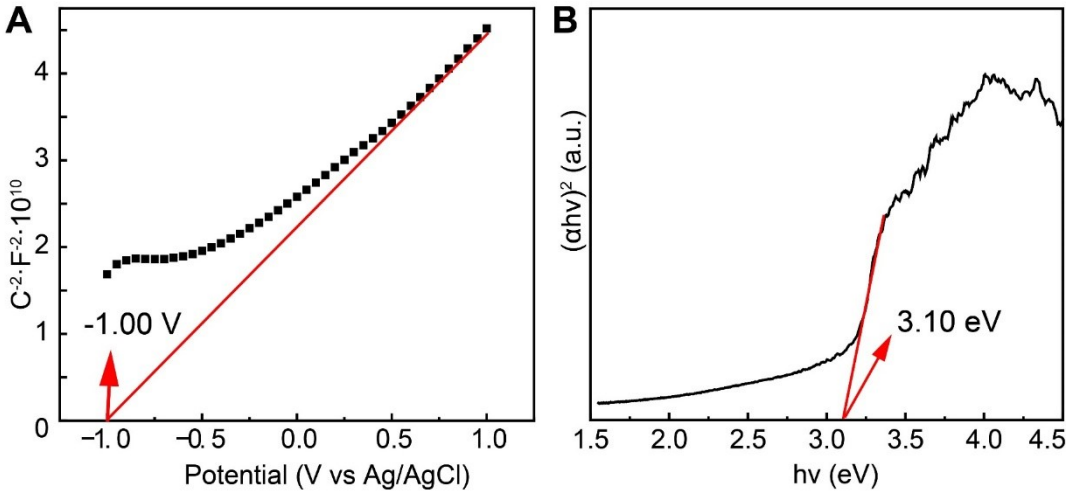

Fig. S18 (A) Mott-Schottky plot of ZnOA; (B) Plot of transformed Kubelka-Munk function versus photon energy in ZnOA.

To study the mineralization of BG after degradation, total organic carbon (TOC) was carried out. The results of TOC before and after the 80 mins degradation of BG by the Al/ZnOA/Ag-Cu are 11.79 mg·L^{-1} and 2.06 mg·L^{-1}, respectively. The TOC removal percentage is calculated by following the equation:[33]

$$TOC\ Reduction\ (\%) = \frac{Initial\ TOC - Final\ TOC}{Initial\ TOC} \times 100\%$$

Results show that the remove efficiency of TOC is as high as 80.83 % within 80 mins in presence of the Al/ZnOA/Ag-Cu, further confirms that lots of BG molecules should be photodegraded into CO_2 and H_2O within 80 mins of illumination.

References

1 C. Liu, Y. Q. Xie, Y. Z. Jiao, Y. J. Du, Q. M. Zheng and Y. X. Sun, *Front. Environ. Sci.*, 2022, **10**, 1065770-1065784.

2 Z. T. Sun, X. H. Fang, C. Kang, Y. Han, L. Zha and X. P. Zhang, *ACS Appl. Nano Mater.*, 2022, **6**, 714-719.

3 Y. Cheng, W. Z. Wang, L. Z. Yao, J. Wang, H. S. Han, T. Y. Zhu, Y. J. Liang, J. L. Fu and Y. N. Wang, *Colloids Surf. A Physicochem. Eng. Aspects*, 2020, **607**, 125507-125515.

4 T. -G. Tran, N. H. Ly, T. T. Nguyen, S. J. Son, Y. Vasseghian, S. -W. Joo and R. Luque,

Environ. Pollut., 2023, **325**, 121441-121449.

5 H. R. Wu, J. J. Wang, Q. Yang, S. X. Qin, Z. X. Li, Y. Zhang, J. Q. Pan and C. R. Li, *Appl. Surf. Sci*., 2023, **621**, 156873-156881.

6 M. S. Yang, J. Yu, F. C. Lei, H. Zhou, Y. S. Wei, B. Y. Man, C. Zhang, C. H. Li, J. F. Ren and X. B. Yuan, *Sens. Actuators B Chem.*, 2018, **256**, 268-275.

7 C. Y. Huang, C. X. Xu, J. F. Lu, Z. H. Li and Z. S. Tian, *Appl. Surf. Sci*., 2016, **365**, 291-295.

8 J. Singh and R. K. Soni, *Colloids Surf. A Physicochem. Eng. Aspects*, 2021, **626**, 127005-127017.

9 X. J. Wang, X. P. Zhu, Y. F. Tao, E. J. Zhang and X. D. Ren, *Spectrochim. Acta. A Mol. Biomol. Spectrosc*., 2023, **290**, 122277-122286.

10 G. W. Su, L. P. Dang, G. Z. Liu, T. Y. Feng, W. Wang, C. G. Wang and H. Y. Wei, *Spectrochim. Acta. A Mol. Biomol. Spectrosc*., 2022, **270**, 120818-120826.

11 Y. L. Wang, D. Li, P. C. Li, W. D. Wang, W. Ren, S. J. Dong and E. K. Wang, *J. Phys. Chem. C*, 2007, **111**, 16833-16839.

12 D. Davis, E. Portelius, Y. Zhu, C. Feigerle and K. D. Cook, *Anal. Chem*., 2005, **77**, 8151-8154.

13 S. Fateixa, H. I. S. Nogueira and T. Trindade, *ACS Omega*, 2018, **3**, 4331-4341.

14 W. Y. Yang, J. Q. Tang, Q. H. Ou, X. Q. Yan, L. Liu and Y. k. Liu, *ACS Omega*, 2021, **6**, 27271-27278.

15 M. Saeed, K. Albalawi, I. Khan, N. Akram, I.H.A. Abd El-Rahim, S.K. Alhag, A. Ezzat Ahmed, Faiza, *Alex. Eng. J.*, 2023, **65**, 561-574.

16 A. Jose, S. D. K. R. Pai, D. Pinheiro, K. Kasinathan, *Environ. Sci. Pollut. Res*., 2021, **28**, 52202-52215.

17 A. Padmanaban, G. Murugadoss, N. Venkatesh, S. Hazra, M. Rajesh Kumar, R. Tamilselvi, P. Sakthivel, *J. Environ. Chem. Eng*., 2021, **9**, 105976-105992.

18 G. Murugadoss, S. Salla, M.R. Kumar, N. Kandhasamy, H. Al Garalleh, M. Garaleh, K. Brindhadevi, A. Pugazhendhi, *Environ. Res*., 2023, **220**, 115171-115180.

19 B. Abarna, T. Preethi, G.R. Rajarajeswari, *J. Environ. Chem. Eng*., 2019, **7**, 102742-102748.

20 M. Muslim, M. Ahmad, M. Jane Alam, S. Ahmad, *Sep. Purif. Technol*., 2023, **315**, 123598-123614.

21 A. Priyadharsan, R. Ranjith, N. Karmegam, G. Thennarasu, S. Ragupathy, T. Hwan Oh, S. Ramasundaram, *Chemosphere*, 2023, **330**, 138708-138715.

22 K. Mahmood, U. Amara, S. Siddique, M. Usman, Q. Peng, M. Khalid, A. Hussain, M. Ajmal, A. Ahmad, S.H. Sumrra, Z.-P. Liu, W.S. Khan, M.N. Ashiq, *J. Nanostruct. Chem*., 2021, **12**, 329-341.

23 M. Bhaumik, A. Maity, H.G. Brink, *J. Colloid Interface Sci*., 2022, **611**, 408-420.

24 S. Ragupathy, A. Priyadharsan, M.S. AlSalhi, S. Devanesan, L. Guganathan, M. Santhamoorthy, S.C. Kim, *Environ. Res*., 2022, **210**, 112833-112841.

25 Y. F. Wang, M. Zhang, H. Yu, Y. Zuo, J. Gao, G. He, Z. Q. Sun, *Appl. Catal. B- Environ*., 2019, **252**, 174-186.

26 X. J. Wen, H. Cheng, W. L. Zhang, L. J. You, J. M. Li, *Talanta*, 2024, **266**, 125140-125150.

27 P. F. Geng, G. T. Chen, Y. Wang, F. Mi, Z. Peng, M. Guan, *Chem. Eng. J*., 2026, **530**, 173233-173247.

28 Y. Y. Zhang, L. L. Wang, X. Y. Kong, H. Y. Jiang, F. Zhang and J. S. Shi, *J. Colloid Interface Sci*., 2018, **522**, 29-39.

29 G. W. Su, T. Y. Feng, Z. J. Huang, Y. N. Zheng, W. X. Zhang, G. Z. Liu, W. Wang, H. Y. Wei and L. P. Dang, *Chem. Eng. J*., 2022, **436**, 135119-135130.

30 K. Mahmood, U. Amara, S. Siddique, M. Usman, Q. Peng, M. Khalid, A. Hussain, M. Ajmal, A. Ahmad, S. H. Sumrra, Z. -P. Liu, W. S. Khan and M. N. Ashiq, *J. Nanostruct. Chem.*, 2021, **12**, 329-341.

31 N. Pugazhenthiran, P. Sathishkumar, O. Albormani, S. Murugesan, M. Kandasamy, M.

Selvaraj, S. Suresh, S. K. Kumar, D. Contreras, H. Váldes and R. V. Mangalaraja, *Chemosphere*, 2023, **313**, 137515-137525.

32 S. Balu, Y. -L. Chen, S. -W. Chen and T. C. Yang, K. *Appl. Catal. B Environ.*, 2022, **304**, 120852-120866.

33 V. Korkmaz, N. Yildirim, G. O. Erguven, B. Durmus and Y. Nuhoglu, *Environ. Technol. Innov.*, 2021, **22**, 101535-101544.